Low Cycle Fatigue of a Directionally Solidified Nickel-Based Superalloy: Testing, Characterisation and Modelling

RJ. Kashinga, LG. Zhao, VV. Silberschmidt, F. Farukh, NC. Barnard, MT. Whittaker, D. Proprentner, B. Shollock, G. McColvin

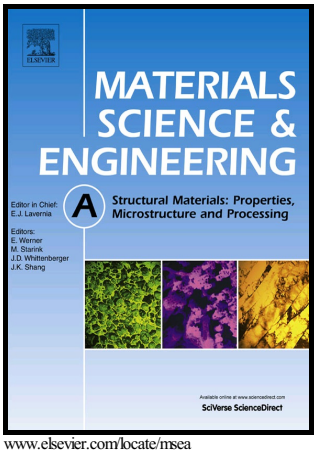

www.elsevier.com/locate/msea

PII: S0921-5093(17)31341-2
DOI: https://doi.org/10.1016/j.msea.2017.10.024
Reference: MSA35627

To appear in: *Materials Science & Engineering A*

Received date: 26 June 2017
Revised date: 4 October 2017
Accepted date: 5 October 2017

Cite this article as: RJ. Kashinga, LG. Zhao, VV. Silberschmidt, F. Farukh, NC. Barnard, MT. Whittaker, D. Proprentner, B. Shollock and G. McColvin, Low Cycle Fatigue of a Directionally Solidified Nickel-Based Superalloy: Testing, Characterisation and Modelling, *Materials Science & Engineering A,* https://doi.org/10.1016/j.msea.2017.10.024

Low Cycle Fatigue of a Directionally Solidified Nickel-Based Superalloy: Testing, Characterisation and Modelling

RJ Kashinga[1], LG Zhao[1*], VV Silberschmidt[1], F Farukh[2], NC Barnard[3], MT Whittaker[3], D Proprentner[4], B Shollock[4] and G McColvin[5]

[1]Wolfson School of Mechanical, Electrical and Manufacturing Engineering, Loughborough University, Loughborough, LE11 3TU, Leicestershire, UK

[2]School of Engineering and Sustainable Development, De Montfort University, Leicester, LE1 9BH, UK

[3]Institute of Structural Materials, College of Engineering, Swansea University, Swansea, SA1 8EN, UK

[4]Warwick Manufacturing Group, University of Warwick, Coventry, CV4 7AL, UK

[5]GE Power, Rugby, Warwickshire, CV21 2NH, UK

*Corresponding author: L.Zhao@Lboro.ac.uk

Abstract

Low cycle fatigue (LCF) of a low-carbon (LC) directionally-solidified (DS) nickel-base superalloy, CM247 LC DS, was investigated using both experimental and computational methods. Strain-controlled LCF tests were conducted at 850°C, with a loading direction either parallel or perpendicular to the solidification direction. Trapezoidal loading-waveforms with 2 s and 200 s dwell times imposed at the minimum and the maximum strains were adopted for the testing. A constant strain range of 2% was maintained throughout the fully-reversed loading conditions (strain ratio R = –1). The observed fatigue life was shorter when the loading direction was perpendicular to the solidification one, indicating an anisotropic

material response. It was found that the stress amplitude remained almost constant until final fracture, suggesting limited cyclic hardening/softening. Also, stress relaxation was clearly observed during the dwell period. Scanning Electron Microscopy fractographic analyses showed evidence of similar failure modes in all the specimens. To understand deformation at grain level, crystal plasticity finite element modelling was carried out based on grain textures measured with EBSD. The model simulated the full history of cyclic stress-strain responses. It was particularly revealed that the misorientations between columnar grains resulted in heterogeneous deformation and localised stress concentrations, which became more severe when the loading direction was normal to a solidification direction, explaining the shorter fatigue life observed.

Keywords: Low cycle fatigue; Directional solidification; Crystal plasticity; Grain misorientations; Stress concentration.

1. Introduction

Nickel based superalloys are widely used as turbine blades and discs in gas turbines operating at high temperatures. The presence, at microstructural level, of $L1_2$ ordered γ'-precipitates in the γ-matrix phase enhances high-temperature mechanical properties of these alloys. These two phases, γ and γ', are typically solid solution strengthened with refractory elements Co, Fe, Mo, W and Ta. Their remarkable high-temperature properties are a result of a combination of various elements in the γ-matrix and γ'-precipitates [1, 2]. These elements also improve the oxidation resistance and reduce γ/γ' mismatch [3-5]. Sizes and morphologies of the strengthening γ'-precipitates are controlled by means of varied manufacturing and heat-treatment processes. Recent studies have shown that mechanical properties are strongly influenced by sizes [2, 6], distribution [7], volume fraction [8,9] and

morphologies [2, 10] of the γ'-precipitates. In addition, grain structures and textures [11] resulting from heat-treatment processes [2, 9, 12] were also found to influence significantly the properties of nickel-based superalloys. In directionally solidified (DS) nickel-based superalloys, preferred crystallographic orientations were obtained with a special casting processes; however, the different growth rates of favourably and unfavourably oriented dendrites led to the growth of grains with different orientations [13].

Columnar grains, aligned with a principal-stress axis, are preferred in turbine blades as they constrain the participation of perpendicularly-oriented grain boundaries in high-temperature fatigue/creep [14]. Compared to the case with a loading axis parallel to the solidification direction, grain boundaries perpendicular to the loading axis affect the deformation behaviour of the material. This results in higher stiffness [5, 15], but fatigue/creep-load bearing capabilities are substantially affected. For temperatures between 650-850°C, tensile and creep behaviour are more dependent on loading direction with respect to that of solidification [16]. Crack-growth behaviour, however, is more sensitive to temperature variations than to changes in the loading direction (with respect to the direction of solidification) [17]. Furthermore, a superior fatigue-life response was reported for specimens with notches oriented normal, as opposed to parallel, to a dendrite-growth orientation [18]. In the work of Shi *et al.* [16] and Moore and Neu [19], the increase in stress concentration around notched regions resulted in decreased fatigue resistance. By using the Basquin and Coffin-Manson empirical relationships, a significantly shorter fatigue life was reported when loading was changed from parallel to 45° orientation with respect to the solidification direction [20]. Moore and Neu [19] also reported that the rate of loading and the imposition of a dwell at maximum/minimum load significantly affected fatigue life at higher temperatures. Such effects were also found for specimens loaded in parallel to the solidification direction.

In recent years, various constitutive models, based on either crystal plasticity or phenomenological formulations have been proposed, to capture various behavioural aspects of nickel-based superalloys. It is noteworthy, however, that most of the models for DS alloys were concentrated on creep and tensile deformation rather than fatigue behaviour. Since crack-growth behaviour showed higher temperature dependency than orientation of the loading direction, the study [17] modified the Paris law to capture this effect by making the stress intensity factor range and the Paris law constant temperature dependent. Predictions based on this modification were then in good agreement with test data for crack growths at temperatures of 600°C and 850°C. Shi *et al.* [16] presented a continuum elasto-viscoplasticity model, which was an extension of the Chaboche constitutive model to capture material rate-dependent and anisotropic deformation behaviour. The model was then applied to study a directionally solidified nickel-based superalloy at 760°C and 850°C, and its results agreed well with experimental data. Crystal plasticity-based modelling was employed to study effects of defects such as carbides, oxides or other particles on fatigue crack initiation. Also Shenoy *et al.* [21] modelled these defects as inclusions resulting in stress concentrations around them which influenced low-cycle-fatigue (LCF) crack nucleation behaviour.

In DS alloys, considerable anisotropy is apparent in material deformation when the loading axis is changed from parallel to perpendicular to the solidification direction. Anisotropy appears to be an inherent characteristic of DS nickel-based superalloys, based on the results reported by other researchers on their deformation [3], fatigue [22] and creep [23] behavior. This was also confirmed in studies based on computational modelling [24, 25]. However, no attempt was made to elucidate a connection between anisotropic behaviour and alloy's microstructure. In previous studies, the grain structures and textures employed were just

assumed and failed to explain the behaviour satisfactorily. Therefore, in this paper, we presented a study of fatigue behaviour of a DS nickel-based superalloy, by employing a combination of testing, microstructural characterisation and numerical modelling. The synergetic influence of imposed dwells (at the maximum and minimum load levels) and varied loading rates on the LCF behavior was particularly studied, for loading both along the solidification direction and normal to it. Using a low-carbon directionally-solidified nickel-based superalloy CM247 LC DS, strain-controlled LCF tests were conducted at two different strain rates and dwell times at an elevated temperature (850°C). To understand the underlying failure mechanism, fracture surfaces were characterised using SEM. In particular, characterisations using EBSD was carried out to establish grain structures and textures, which allowed us, for the 1st time, to consider abnormal grains formed during material processing (a cluster of smaller grains with orientations distinctively different from those of the major columnar grains). Furthermore, these EBSD data were used as input into the finite element (FE) study, and the simulation results were employed to elucidate anisotropic fatigue behaviour observed in the tested specimens.

2. Materials, Testing and Characterisation

2.1 Materials

The material studied in this paper is a DS nickel-based superalloy with a low carbon (LC), content, designated as CM247 LC DS. The chemical composition by weight percentage (wt.%) is shown in Table 1. The studied material underwent a three-stage standard heat treatment process. The first stage was a 2.5 h solution heat treatment at 1246°C, followed by cooling, which resulted in precipitation of a uniform fine γ/γ'-microstructure. The second stage was a 4.5 h heat treatment at 1080°C to yield the optimum size distribution of γ'-precipitates. The final stage was an aging treatment at 870°C for 24 h. The final product had a

density of about 8.32 g/cm^{-3}, with a solvus temperature of 1160°C.

2.2 LCF Tests

Plain cylindrical specimens were machined for this study, with an extensometer gauge length of 12.5 mm and a diameter of 6.4 mm. Four specimens (two types) were prepared, two with the solidification direction aligned with the loading axis (L specimens) while the other two had this direction perpendicular to the axis (T specimens see the schematic drawing in Fig. 1). Uniaxial LCF tests were carried out using an Instron electromechanical test system and high a temperature axial extensometer. Mechanical testing was performed isothermally at 850°C using radiant furnace heating. All tests were carried-out in laboratory air, and 3 N-type thermocouples were used to ensure the temperature gradient across the gauge section was less than 2°C. Two trapezoidal loading waveforms, denoted as 2-2-2-2 and 200-200-200-200, were considered for each type of specimen. Specifically, the test parameters included 2 s or 200 s dwells imposed at both the minimum and the maximum strain levels (see Fig. 2). In all tests, a total strain range of 2.0% and a strain ratio of $R = -1.0$ were applied. To understand the underlying mechanism responsible for the resultant failure modes, post-mortem fractography was performed using a JOEL JSM-7800F Extreme-resolution Analytical Field Emission Scanning Electron Microscope (FE-SEM).

2.3 EBSD analyses

A wire electrical discharge machining (EDM) method was used to cut all four failed specimens across or along the direction of solidification (see Fig. 3), to reveal the grain-structure. To achieve the desired surface finish, mechanical polishing with various GRIT sizes was carried out initially, using 240, 400, 600, and, finally, 1200 GRIT. As grinding alone could not give a good enough finish, further polishing with colloidal silica with discs

having abrasive sizes of 6.0 µm, 1.0 µm and, finally, 0.25 µm, was performed achieving final polished surface with an R_q = 20 nm. Electron Backscatter Diffraction (EBSD) was used to reveal the grain texture to be introduced into numerical modelling.

3. Modelling Work

3.1 Crystal plasticity model

The constitutive behaviour of the material was described using a crystal plasticity theory. The model was based on a multiplicative decomposition of the total (elastic and plastic) deformation gradient **F** into its elastic ($\mathbf{F}^e$) and plastic ($\mathbf{F}^p$) components [28-30]:

$$\boldsymbol{F} = \boldsymbol{F^e F^p}, \quad \ldots [1]$$

where $\mathbf{F}^e$ describes the elastic response (stretching and rigid-body rotation) of the crystals while the crystallographic slip along slip planes due to dislocation motion is described by $\mathbf{F}^p$. Here, octahedral slip is taken as the dominant plastic deformation process. The rate of plastic deformation gradient $\dot{\boldsymbol{F}}^{\boldsymbol{p}}$ was expressed in terms of a shear strain rate as [28-30]

$$\dot{\boldsymbol{F}}^p = \boldsymbol{L}^p \boldsymbol{F}^p \text{ hence } \boldsymbol{L}^p = \dot{\boldsymbol{F}}^p (\boldsymbol{F}^p)^{-1} = \sum_{\alpha=1}^{N} \dot{\gamma}^\alpha (\boldsymbol{m}^\alpha \otimes \boldsymbol{n}^\alpha), \quad \ldots [2]$$

where $\dot{\gamma}^\alpha$ is the shear strain rate on the slip system α, $\boldsymbol{m}^\alpha$ and $\boldsymbol{n}^\alpha$ are orthonormal unit vectors defining the slip direction and the slip plane normal, respectively. The parameter N is the number of active slip systems.

To describe the shear deformation on slip systems, two internal and scalar state variables per slip system were considered - slip resistance (S^α), an isotropic hardening variable, and back stress (B^α), a kinematic hardening variable. The flow rule, i.e., the resolved shear strain rate ($\dot{\gamma}^{\boldsymbol{\alpha}}$), for each slip system at a given a temperature (θ), was therefore expressed as

$$\dot{\gamma}^{\alpha} = \dot{\gamma}_0 \exp\left[\frac{-F_0}{\kappa\theta}\left\langle 1 - \left\langle \frac{\left|\tau^{\alpha} - B^{\alpha}\right| - S^{\alpha}\frac{\mu}{\mu_0}}{\hat{\tau}_0 \frac{\mu}{\mu_0}} \right\rangle^{p} \right\rangle^{q}\right] \mathrm{sgn}(\tau^{\alpha} - B^{\alpha}), \quad \ldots [3]$$

where κ is the Boltzmann constant, τ^{α} is the resolved shear stress on the slip system α, θ is the absolute temperature, μ and μ_0 are the shear moduli at temperatures θ and 0 K, respectively, and F_0, $\hat{\tau}_0$, p, q and $\dot{\gamma}_0$ are material constants, whose values depend on the slip system family.

The slip resistance on a generic slip system evolves according to the following relation:

$$\dot{S}^{\alpha} = [h_S - d_D(S^{\alpha} - S_0^{\alpha})]\,|\dot{\gamma}^{\alpha}|, \quad \ldots . [4]$$

where the first and second terms are the static and dynamic recovery terms associated with the material constants, h_S and d_D, respectively, S_0^{α} is the initial slip resistance. The back stress evolves according to a standard hardening-dynamic recovery format:

$$\dot{B}^{\alpha} = h_B\dot{\gamma}^{\alpha} - r_D B^{\alpha}|\dot{\gamma}^{\alpha}|, \quad \ldots . [5]$$

where h_B is the hardening constant and r_D is the dynamic recovery function.

The model was implemented numerically into a FE code ABAQUS via a user-defined material subroutine (UMAT), using the fully implicit integration algorithm. Two slip system families (both octahedral and cubic) were used to describe inelastic deformation in some recently published work [22, 30, 31]. However, the contribution from the cubic slip system is very limited for nickel based superalloy, therefore this study only considered one slip system family, i.e., twelve (12) octahedral ({111}<110>) slip systems. As such, the model was considerably simplified as only one set of paramters was needed to describe the cyclic deformation behaviour of CM247 LC DS.

3.2 Finite element study

3.2.1 Model development

Recent studies with this model employed in describing anisotropic material deformation behaviour considered only artificially created textures [5, 16, 17]. This study, however, utilised realistic representations of grain sizes and orientations, determined using the EBSD technique. Therefore, FE models were developed based on the actual grain morphologies and textures obtained from EBSD analyses of failed fatigue specimens, see Figs. 7 and 9. To reduce computing times, only a fraction of the gauge length - 2 mm out of the 12.5 mm - was considered for both L and T specimens. Using MATLAB, grain boundaries in EBSD images were digitised providing two-dimensional co-ordinates in a csv format. These co-ordinates were then used to generate ABAQUS-readable data, from a PYTHON script, for developing FE models. Grain orientations were defined using Euler angles also established with EBSD.

3.2.2 Boundary and loading conditions

To avoid rigid-body motion, loading in parallel to the solidification direction was achieved by applying a pin-restraint at a centre node of the bottom face of the FE model, while the whole model face was restricted from any displacements along the loading direction (the z-axis). Uniaxial strain-controlled fully reversed ($R = -1$) loading conditions, with frequencies shown in Fig. 2, were employed. This was achieved by applying cyclic displacements, with an equivalent total strain of 2% in the z-direction, on the free face. For specimens loaded perpendicular to the solidification direction, the developed FE models were constrained by applying a pin-restraint on a node central to the semi-circular face. Based on the sign convention used in the EBSD analyses, illustrated schematically in Fig. 1, the FE models were restricted from displacements along the loading direction (the x-axis). For symmetry,

the semi-cylindrical FE model was restricted from displacements along the y-axis. Uniaxial strain-controlled fully reversed loadings, with regimes presented in Fig. 2, were then applied at the top face.

3.2.3 Post-processing of stress-strain results

Due to the difference in grain sizes and shapes, non-uniform mesh elements were employed in local regions. To obtain the material's global stress-strain response by means of homogenization, the following volume integrals were used:

$$\bar{\sigma}_{ij} = \frac{1}{V}\int \sigma_{ij}\, dV, \qquad \ldots [6]$$

$$\bar{\varepsilon}_{ij} = \frac{1}{V}\int \varepsilon_{ij}\, dV, \qquad \ldots [7]$$

where $\bar{\sigma}_{ij}$ and $\bar{\varepsilon}_{ij}$ are the average stresses and strains, respectively, for individual elements in the FE model, V is the element's volume and σ_{ij} and ε_{ij} are the local stresses and strains for each element. These integrals were computed using the Gauss integration algorithm in ABAQUS. A post-processing subroutine was therefore written in FORTRAN, interfaced with the finite element (FE) code ABAQUS, to obtain the magnitudes of global stresses and strains from respective local values at integration points of all elements.

4. Results

4.1 Low cycle fatigue behaviour

For the specimens considered in this study, the LCF life measured in our tests showed considerably high orientation and strain-rate dependencies. This was evident in the significantly longer fatigue life observed in specimens loaded along the solidification direction as compared to those loaded normal to it. In the former case, a reduction in the strain rate by a factor of 100 reduced the fatigue life nearly fourfold. In contrast, in the latter

case, this reduction was approximately twofold, see Fig. 4. Deformation was characterised by limited cyclic hardening/softening, as evident from the stabilised evolution of stress amplitudes to failure for all the specimens (Fig. 8). Additionally, significant stress relaxation during dwells at the minimum and maximum strain was observed in all the specimens considered in this study.

4.2 Fracture surface examination

To establish the predominant failure mode in this study, fracture surfaces were analyzed using scanning electron microscopy (SEM). At relatively low magnification, no measurable changes in cross-sectional area were observed with FEG-SEM at the point of fracture when compared to the gauge-length section. At higher magnification, similar fracture surface features were revealed in all the specimens, as shown in Figs. 5(a)-(d); these included flat planes and cleavage-like dominated separated by sharp edges. These features were, however, more observable in the specimen subjected to 2s-2s-2s-2s loading waveform parallel to the solidification direction, Fig. 5 (a). Fracture surface features were indicative of failure dominated by brittle fracture.

It was further observed that, in all the specimens, fracture surfaces were mostly normal to the loading axis. Several crack initiation sites were observed, especially at high strain rates. Such multiple initiation points could have resulted from the internal and surface pores. Also, low-level reduction of specimen's cross-sectional area at the fracture sites was observed. Literature recognises that cracks normally originate from manufacturing defects and other stress-concentration points. The characteristic features observed [31] are related to the growth and final fracture results, and the breaking of atomic bonds along specific crystallographic planes. In specimens loaded along the solidification direction, the observed fracture surface

features were possibly caused by transgranular cracking, since fracture occurred normal to the direction of solidification. On the other hand, a combination of intergranular and transgranular cracking would prevail in specimens where loading was normal to the solidification direction, since fracture occurred in the direction of grain boundaries. Similar behaviour was reported by other studies [16, 17] investigating fatigue behaviour of directionally solidified nickel-based superalloys.

4.3 EBSD characterization

All the specimens were characterised using EBSD based on the sign convention of the axes in Fig. 1. Non-uniform distribution of grain sizes and orientations were the common characteristics of the analysed microstructures. The largest grains were observed in the L specimen while the smallest sizes were in the 200s-200s-200s-200s T one. Ideally, the columnar grain structure (directional solidification) should follow a single lattice orientation, e.g. $\langle 001 \rangle$. However, the specimens used in this study were machined from slabs with variation in grain size and misorientation between grains. The effects of solidification cooling systems and competitive grain growth were recognised as the cause for these characteristic features [13,32]. A grain width had a range from 5 to 2500 μm for the specimens with loading direction parallel to the solidification direction. In T specimens, this parameter ranged from 5 to 750 μm.

Crystallographic orientations of grains were defined using the Euler angles obtained through EBSD analyses, which had mean values of $[260 \pm 92, 11 \pm 6, 32 \pm 21]$. These angles were close to those for the $\langle 001 \rangle$ crystallographic orientation, as can be seen from the inverse pole figures in Fig. 6. Based on Schmid's law [33], the Schmid factor can be derived in terms of Euler angles as

$$\tau_{RSS} = \sigma \sin\Phi \sin\phi_2 \cos\Phi \quad \text{... [8]}$$

where τ_{RSS} is the resolved shear stress on slip planes and along slip directions, σ is the applied stress, Φ and ϕ_2 are the second and the third Euler angles, respectively, in the Bunge notation. Therefore, grains with orientations far from ⟨001⟩ but close to the ⟨111⟩ orientations (i.e. far from $\Phi = 0$ and $\phi_2 = 0$, but close to $\Phi = 54.7$ and $\phi_2 = 45$), will have a higher initial Schmid factor, which could lead to a higher resolved shear stress, τ_{RSS}. When the resolved shear stress τ_{RSS} reached a critical value, slip began and the grain started to yield in deformation. Therefore, grains with orientations far from ⟨001⟩ but close to the ⟨111⟩ orientations are more likely to yield earlier than the rest. In this study, this deviation in orientation for certain grains was found to be among the causes for the inferior fatigue-life behaviour as discussed in the following modelling work.

4.4 Crystal plasticity modelling

4.4.1 FE model and parameter calibration

Although there were many grains in specimens with the loading direction perpendicular to the solidification direction, only a small section of length 2.0 mm was considered for FE simulation in this study as indicated in Fig. 6 (c) and (d) to reduce computing times. Specifically, the numbers of grains considered in the FE models were 6, 45, 27 and 112 for cases (a), (b), (c) and (d), respectively. These FE models, developed from the actual grain microstructures and texture, were meshed with quadratic tetrahedral elements – C3D10 (Fig. 7). Each grain orientation was defined in the user-subroutine (UMAT), using three Euler angles (measured via EBSD) and incorporated into the FE model.

With the imposed boundary conditions (see Section 3.2.2), FE simulations were carried out to calibrate the model parameters against the available experimental data. The orientation-dependent anisotropic stiffness constants C_{11}, C_{12} and C_{44} were determined first by considering the elastic deformation only. Full monotonic stress-strain response was then considered to adjust parameters p, q, F_0, $\hat{\tau}_0$, S_0 and f_C of the model controlling plastic deformation. The starting-point values for these parameters were sought in literature [28–30]. Then, the first stress-strain cyclic loop with stress-relaxations during dwell times was considered for re-adjustment of p, q and $\hat{\tau}_0$. Finally, cyclic-stress evolution to final failure was considered to refine model parameters h_S, h_B, d_D and r_D that control cyclic hardening/softening behaviour of the material. Table 2 summarises the values of all model parameters that were calibrated.

The parameters given in Table 2 are close to those in the literature [22, 30, 31, 35], with an exception of p, q and $\hat{\tau}_0$. The difference is attributed to considerable amount of stress relaxations during the dwell periods at the minimum and maximum strains observed in this study. The consideration of only one slip system family (the octahedral slip system) further contributed to this. The anisotropic ratio, a parameter defined as $(C_{11} - C_{12})/2C_{44}$, normally lies in the normal range between 0 and 1. When the ratio is close to 0, material is more anisotropic. In the current study, a value of about 0.25 was found, indicating orientation-dependent behaviour of the material.

4.4.2 Stress-strain Response

From the averaging method based on the volume-integral approach (Section 3.2.3), the global stress-strain response was obtained. Fig. 8 compares cyclic stress-strain responses obtained with numerical simulations and the test data for all four specimens. These results showed that

the material had higher stiffness when load was normal to the solidification direction. This was attributed to the presence of grain boundaries perpendicular to the loading direction which inhibit the mobility of dislocations. In this loading direction, grain-boundary deformation is normally different from that in the grain bulk due to constrains between neighbouring grains. Therefore, for the aggregate grain and grain-boundary structure to deform uniformly, grain boundary compatibility between adjacent grains should prevail. Strain components on either side of the boundary need to be equal for slip to occur without relative sliding of the boundary between the adjacent grains. Additionally, since deformation of crystals cannot start at the primary slip system, strain compatibility between the neighbouring crystals and the grain boundaries should exist. As a result, repulsive forces exerted on successive dislocations result pile-ups at grain boundaries and, hence higher stiffness [36, 37]. Orientation-dependent deformation behaviour observed in this study are consistent with the findings of Dong et al.[3] and Shi et al. [16].

The numerical simulation results based on the crystal-plasticity model with parameters from Table 2 showed a good agreement with the test data. The model successfully predicted the stress-strain responses for cyclic loops, evolution of stress amplitudes to failure, stress-relaxation during dwells at minimum and maximum strains and stabilized cyclic hardening/softening. Additionally, the difference in stiffness between specimens loaded parallel and perpendicular to their solidification directions was successfully predicted. Stresses and strains for the four developed FE models, calculated by the averaging approach in Eqs. 6 and 7, were plotted and compared with the respective experimental data in Fig. 8. The first-cyclic stress-strain loops and the stress-evolution to failure are presented in these plots. Significant stress-relaxation is clearly observable during the dwell periods imposed at the minimum and maximum strain levels.

4.4.3 Stress distribution

The FE numerical simulations in this study were based on actual grain structures and orientations provided by EBSD analyses. Under strain-controlled loading conditions, all developed FE models were subjected to the same displacement. Based on EBSD characterisation, grains inclined to the ⟨001⟩ crystallographic orientation had higher initial Schmid factors. Depending on the extent of this misorientation, the numerical simulations with the developed FE models revealed significantly higher local stresses in such grains. Based on the EBSD characterisation results presented in Fig. 6 (a), the high misorientations between the grains observed in the specimen subjected to the 2s-2s-2s-2s load-waveform only led to higher stresses along the grain boundary, this could be result of the different grain sizes. Such a response was more pronounced in the FE models subjected to loads normal to the solidification direction, where grain misorientations led to significantly high localisation of stresses. Also, the stresses were higher and more non-uniform for specimens loaded normal to the solidification direction, justifying their shorter fatigue life (Fig. 9).

Since numerical simulations in this study were based on the actual grain structures and orientations established with the aid of EBSD analyses, the influence of individual grain orientation on stress distribution could be investigated appropriately. The specimen subjected to the 200s-200s-200s-200s loading waveform (parallel to solidification direction) was chosen to elucidate the dependency of stress distribution on grain orientation. The Euler angles for all the grains, obtained from EBSD analyses, were used to determine the Schmid factors based on Eq. 8 [39, 40]; a plot of these Schmid factors is given in Fig. 10. Seven grains with the highest Schmid factors were identified, highlighted and labelled in both Figs. 9b and 10. These grains exhibited high levels of stresses in the contour plot of von Mises

stress when compared to the rest of the grains. Euler angles defining orientations for these seven grains are given in Table 3. Similar behaviour was also observed in other specimens (see Fig. 9 (a), (c) and (d)). As such, it was concluded that grain misorientation was a determining factor for local stress concentration as observed in Fig. 9. In fact, specimens with the loading direction perpendicular to the solidification direction had several highly-misorientated grains (i.e. high Schmid factors), which introduced severe local stress concentrations and resulted in specimens being more prone to failure. This view is supported by the observed shorter fatigue life as presented in Figs. 4 and 8.

Columnar grains in DS alloys, aligned along a principal-stress axis, are preferred as they constrain the participation of perpendicularly-oriented grain boundaries in load bearing. The technique is widely employed in the design and manufacture of materials applied in ambient and non-ambient environments, including Co-based [39], Fe-based [40] and Al-based [41] alloys. Our method is surely applicable to these alloy systems, and just requires a calibration of the crystal plasticity model against test data and also EBSD measurements for model input. However, the exercise will need significant efforts and time, and is beyond the scope of the current paper. We plan to explore this in our future research, when such an opportunity arises.

5. Conclusions

Low cycle fatigue tests for CM247 LC DS were conducted under strain-controlled conditions at a temperature of 850ºC in laboratory air. The observed results showed stabilised evolution of stress amplitudes to failure for all loading conditions. Stress relaxations during the minimum and maximum strain dwells were observed in all regimes. The results further demonstrated strong anisotropic behaviour in fatigue life, which was both strain rate and

orientation dependent. Cleavage planes with claw-like features were more observable on the fracture surfaces of specimens subjected to a higher strain rates than their counterparts.

The crystal plasticity modelling approach was used to simulate the constitutive behaviour for CM247 LC DS under experimental loading conditions. FE models were developed from the actual microstructure and texture, established by EBSD analyses of the failed specimens. Simulation results for the stress-strain loops and cyclic stress evolution until failure were in good agreement with the experimental data. The model therefore has good prediction capability for high-temperature mechanical behaviour for different crystallographic orientations and strain rates. Localized stress concentration arising from grain misorientation was used to explain the reduced fatigue life in directionally solidified superalloys loaded in a direction normal to the solidification direction.

6. Acknowledgements

The work was funded by the EPSRC (Grants EP/K026844/1 and EP/M000966/1) of the UK, and in collaboration with GE Power, Dstl and Uniper. We acknowledge the University of Southampton for heat treatment of the material (Prof Philippa Reed and Dr Rong Jiang). The crystal plasticity UMAT was originally developed by Professor Esteban Busso, Professor Noel O'Dowd and their associates while they were with the Imperial College, London. Research data for this paper is available on request from the project principal investigator Prof Liguo Zhao (l.zhao@lboro.ac.uk) at Loughborough University.

7. References

[1] J. Nie, Z. Liu, X. Liu, Z. Zhuang, Size effects of γ′ precipitate on the creep properties of directionally solidified nickel-base super-alloys at middle temperature, Comput.

Mater. Sci., 46 (2) (2009) 400-406.

[2] P. Xia, J. Yu, X. Sun, H. Guan, Z. Hu, Influence of γ′ precipitate morphology on the creep property of a directionally solidified nickel-base superalloy, Mater. Sci. and Eng.: A, 476 (1) (2008) 39-45.

[3] C. Dong, X. Yang, D. Shi, H. Yu, Modeling of anisotropic tensile and cyclic viscoplastic behavior of a nickel-base directionally solidified superalloy, Mater. Des. (2014).

[4] A. Jalowicka, Effect of strengthening additions on the oxidation and sulphidation resistance of cast Ni-base superalloys, No. RWTH-CONV-144,023th Faculty of Mechanical Engineering, 2013.

[5] R. Reed, T. Tao, N. Warnken, Alloys-by-design: application to nickel-based single crystal superalloys, Acta Mater. 57 (19) (2009) 5898-5913.

[6] M.. Acharya, G.. Fuchs, The effect of long-term thermal exposures on the microstructure and properties of CMSX-10 single crystal Ni-base superalloys, Mater. Sci. Eng. A. 381 (2004) 143–153.

[7] T. Sugui, T. Ning, Y. Huichen, M. Xianlin, L. Ying, Influence of solution temperature on microstructure and creep property of a directional solidified nickel-based superalloy at intermediate temperatures, Mater. Sci. Eng. A. 615 (2014) 469–480.

[8] T. Murakumo, T. Kobayashi, Y. Koizumi, H. Harada, Creep behaviour of Ni-base single-crystal superalloys with various γ′ volume fraction, Acta Mater. 52 (2004) 3737–3744.

[9] T. Pollock, S. Tin, Nickel-based superalloys for advanced turbine engines: chemistry, microstructure and properties, J. Propul. Power, 22 (2) (2006) 361-374.

[10] L. Shui, T. Jin, S. Tian, Z. Hu, Influence of precipitate morphology on tensile creep of a single crystal nickel-base superalloy, Mater. Sci. Eng. A. 454–455 (2007) 461–466.

[11] D. Chatterjee, N. Hazari, N. Das, R. Mitra, Microstructure and creep behavior of DMS4-type nickel based superalloy single crystals with orientations near ⟨001⟩ and ⟨011⟩, Mater. Sci. Eng. A. 528 (2010) 604–613.

[12] P. Caron, T. Khan, Improvement of creep strength in a nickel-base single-crystal superalloy by heat treatment, Mater. Sci. Eng. 61 (2) (1983) 173-184.

[13] Y.Z. Zhou, A. Volek, N.R. Green, Mechanism of competitive grain growth in directional solidification of a nickel-base superalloy, Acta Mater. 56 (2008) 2631–2637.

[14] S. Gao, M. Rajendran, M. Fivel, Primary combination of phase-field and discrete dislocation dynamics methods for investigating athermal plastic deformation in various realistic Ni-base single crystal, Modell. Simul. Mater. Sc. Eng. 23 (7) (2015) 075003.

[15] I. Vladimirov, S. Reese, G. Eggeler, Constitutive modelling of the anisotropic creep behaviour of nickel-base single crystal superalloys, Int. J. Mech. Sci. 51 (4) (2009) 305-313.

[16] D.Q. Shi, X.A. Hu, J.K. Wang, H.C. Yu, X.G. Yang, J. Huang, Effect of notch on fatigue behaviour of a directionally solidified superalloy at high temperature, Fatigue Fract. Eng. Mater. Struct. 36 (2013) 1288–1297.

[17] X. He, Y. Zhang, H. Shi, J. Gu, C. Li, Influence of orientation and temperature on the fatigue crack growth of a nickel-based directionally solidified superalloy, Mater. Sci. Eng: A 618 (2014) 153-160.

[18] P. Xia, L. Yang, J. Yu, X. Sun, H. Guan, Z. Hu, Influence of direction of notch on thermal fatigue property of a directionally solidified nickel base superalloy, Rare Met. 30 (2011) 472-476.

[19] Z.J. Moore, R.W. Neu, Creep fatigue of a directionally solidified Ni-base superalloy - smooth and cylindrically notched specimens, Fatigue Fract. Eng. Mater. Struct. 34

(2011) 17–31.

[20] M. Marchionni, G.A. Osinkolu, M. Maldini, High temperature cyclic deformation of a directionally solidified ni-base superalloy, Fatigue Fract. Eng. Mater. Struct. 19 (1996) 955–962.

[21] M. Shenoy, R. Kumar, D. McDowell, Modeling effects of nonmetallic inclusions on LCF in DS nickel-base superalloys, Int. J. Fatigue. 27 (2) (2005) 113-127.

[22] R.A. Kupkovits, R.W. Neu, Thermomechanical fatigue of a directionally-solidified Ni-base superalloy: Smooth and cylindrically-notched specimens, Int. J. Fatigue. 32 (2010) 1330–1342.

[23] Z. Yue, Z. Lu, C. Zheng, Evaluation of creep damage behavior of nickel-base directionally solidified superalloys with different crystallographic orientations, Theor. Appl. Fract. Mech. (1996).

[24] D. Shi, C. Dong, X. Yang, Constitutive modeling and failure mechanisms of anisotropic tensile and creep behaviors of nickel-base directionally solidified superalloy, Mater. Des. (2013).

[25] J. Huang, X. Yang, D. Shi, H. Yu, C. Dong, X. Hu, Systematic methodology for high temperature LCF life prediction of smooth and notched Ni-based superalloy with and without dwells, Comput. Mater. Sci. 89 (2014) 65–74.

[26] E.P. Busso, Cyclic deformation of monocrystalline nickel aluminide and high temperature coatings, Diss. Massachusetts Institute of Technology, (1990).

[27] E. Busso, F. McClintock, A dislocation mechanics-based crystallographic model of a B2-type intermetallic alloy, Int. J. Plast. 12 (1) (1996) 1-28.

[28] R. Dennis, Mechanistic modelling of deformation and void growth behaviour in superalloy single crystals, Diss. Imperial College London, (2000).

[29] B. Lin, L. Zhao, J. Tong, A crystal plasticity study of cyclic constitutive behaviour,

crack-tip deformation and crack-growth path for a polycrystalline nickel-based superalloy, Eng. Fract. Mech. 78 (10) (2011) 2174-2192.

[30] A. Karabela, L. Zhao, B. Lin, Oxygen diffusion and crack growth for a nickel-based superalloy under fatigue-oxidation conditions, Mater. Sci. and Eng: A, 567 (2013) 46-57.

[31] W. Callister, D. Rethwisch, Fundamentals of materials science and engineering, John Wiley & Sons. 2013.

[32] T.M. Pollock, W.H. Murphy, E.H. Goldman, D.L. Uram, J.S. Tu, Grain defect formation during directional solidification of nickel base single crystals, Superalloys 1992 (1992): 125-134.

[33] U. Messerschmidt, Dislocation Dynamics During Plastic Deformation, Springer Science & Business Media, 2010.

[34] F. Farukh, L. Zhao, R. Jiang, P. Reed, Realistic microstructure-based modelling of cyclic deformation and crack growth using crystal plasticity, Comput. Mater. Sci. 111 (2016) 395-405.

[35] M. Shetty, Dislocations and mechanical behaviour of materials, PHI Learning Pvt. Ltd. 2013.

[36] G. Dieter, D. Bacon, Mechanical metallurgy, SI metric edition. 1986.

[37] U.F. Kocks, C.N. Tomé, H.-R. Wenk, Texture and Anisotropy: Preferred Orientations in Polycrystals and Their Effect on Materials Properties, Cambridge University Press, 2000.

[38] H.-J. Bunge, Texture Analysis in Materials Science: Mathematical Methods, Elsevier, 2013.

[39] W.H. Jiang, H.R. Guan, Z.Q. Hu, Effects of heat treatment on microstructures and mechanical properties of a directionally solidified cobalt-base superalloy, Mater. Sci.

Eng. A. 271 (1999) 101–108.

[40] P.M. Milenkovic S, Microstructure and mechanical properties of directionally solidified Fe–Al–Nb eutectic, Intermetallics. Volume 16 (2008) 1212–1218.

[41] E. Çadırlı, U. Büyük, S. Engin, H. Kaya, Effect of silicon content on microstructure, mechanical and electrical properties of the directionally solidified Al–based quaternary alloys, J. Alloys Compd. 694 (2017) 471–479.

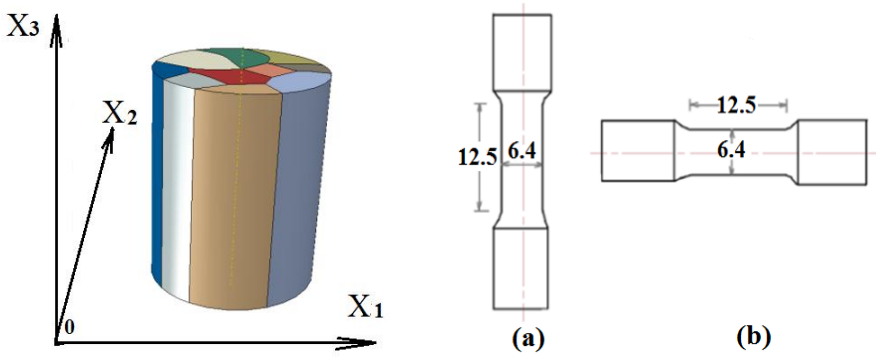

Figure 1, Schematic diagram showing two orientations of specimen with loading direction coincident (a) or normal (b) to the direction of solidification (dimensions in mm).

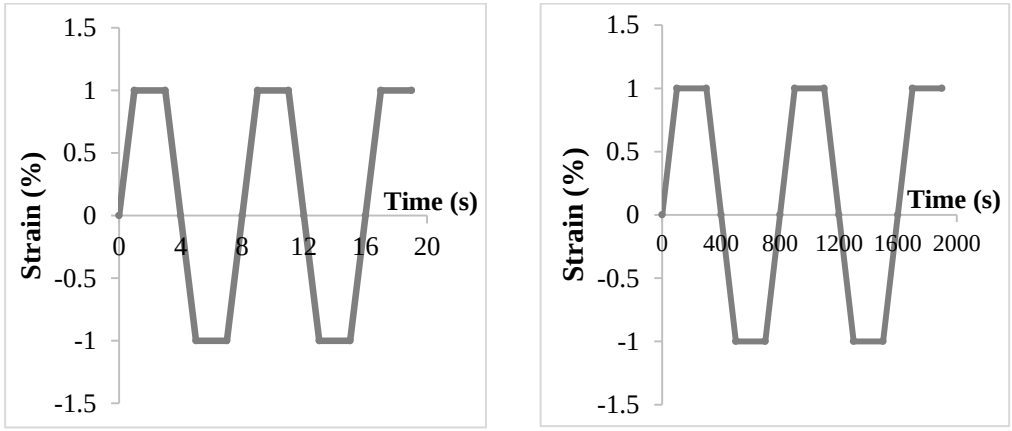

(a) **(b)**

Figure 2, Schematics of loading waveforms used: (a) 2s-2s-2s-2s, (b) 200s-200s-200s-200s

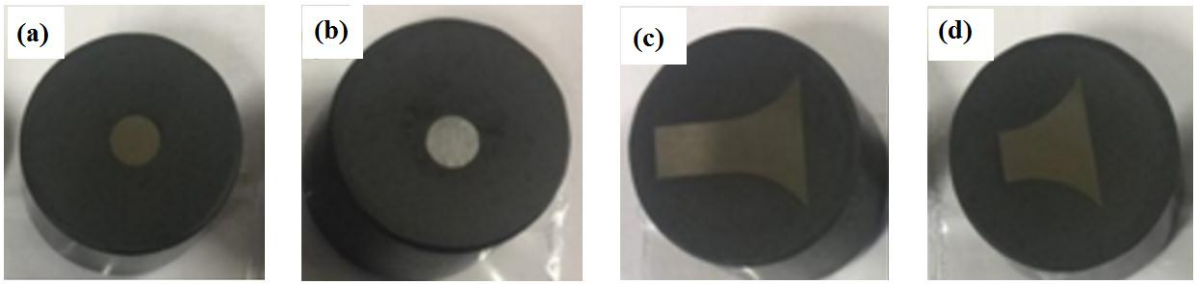

Figure 3, Specimens for EBSD analyses, embedded in conductive resin: (a) 2s-2s-2s-2s (parallel to solidification direction); (b) 200s-200s-200s-200s (parallel to solidification direction); (c) 2s-2s-2s-2s (perpendicular to solidification direction); (d) 200s-200s-200s-200s (perpendicular to solidification direction).

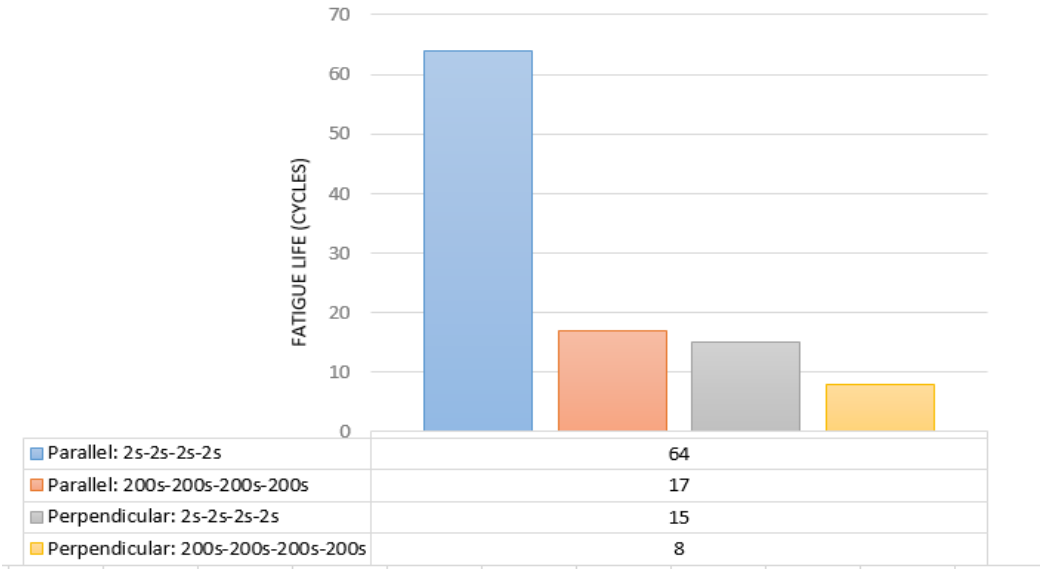

Figure 4, Low cycle fatigue life for various loading waveforms and directions.

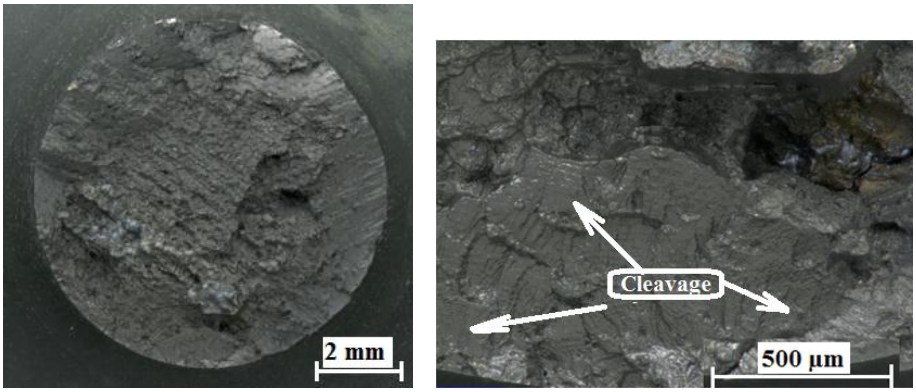

(a)

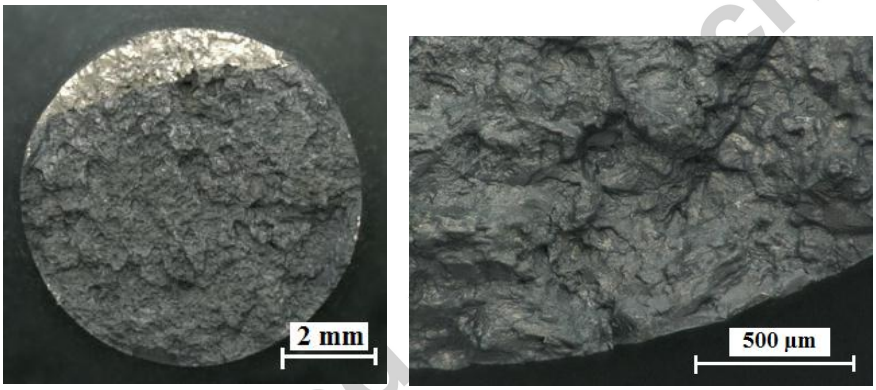

(b)

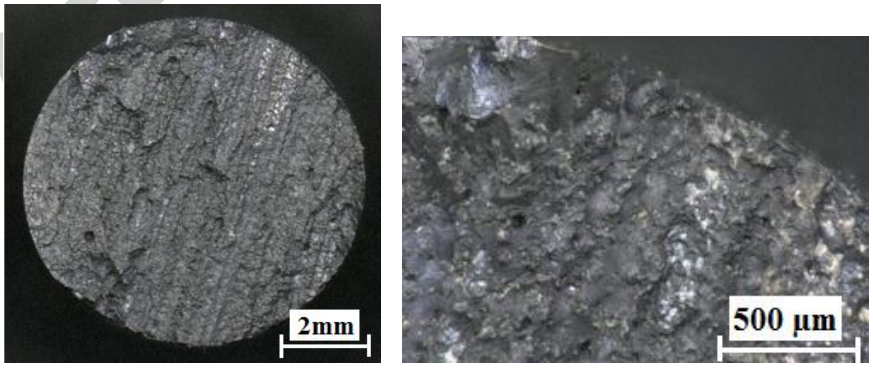

(c)

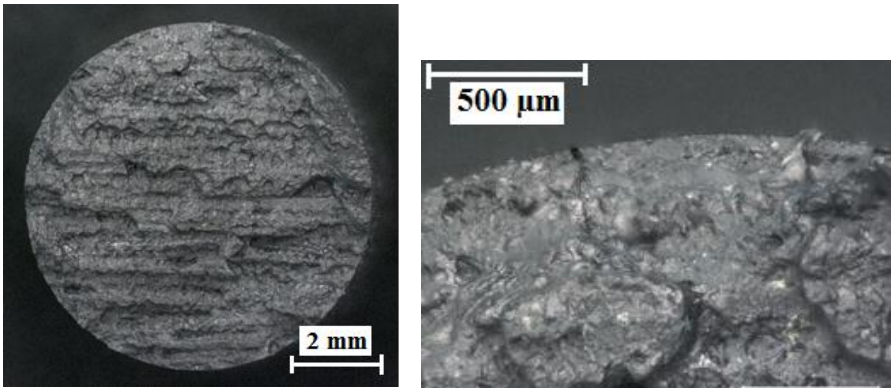

(d)

Figure 5, SEM fractography of fatigue tested specimens subjected to 2s-2s-2s-2s (a and c) and 200s-200s-200s-200s (b and d) loading waveforms parallel (a and b) and perpendicular (c and d) to solidification direction.

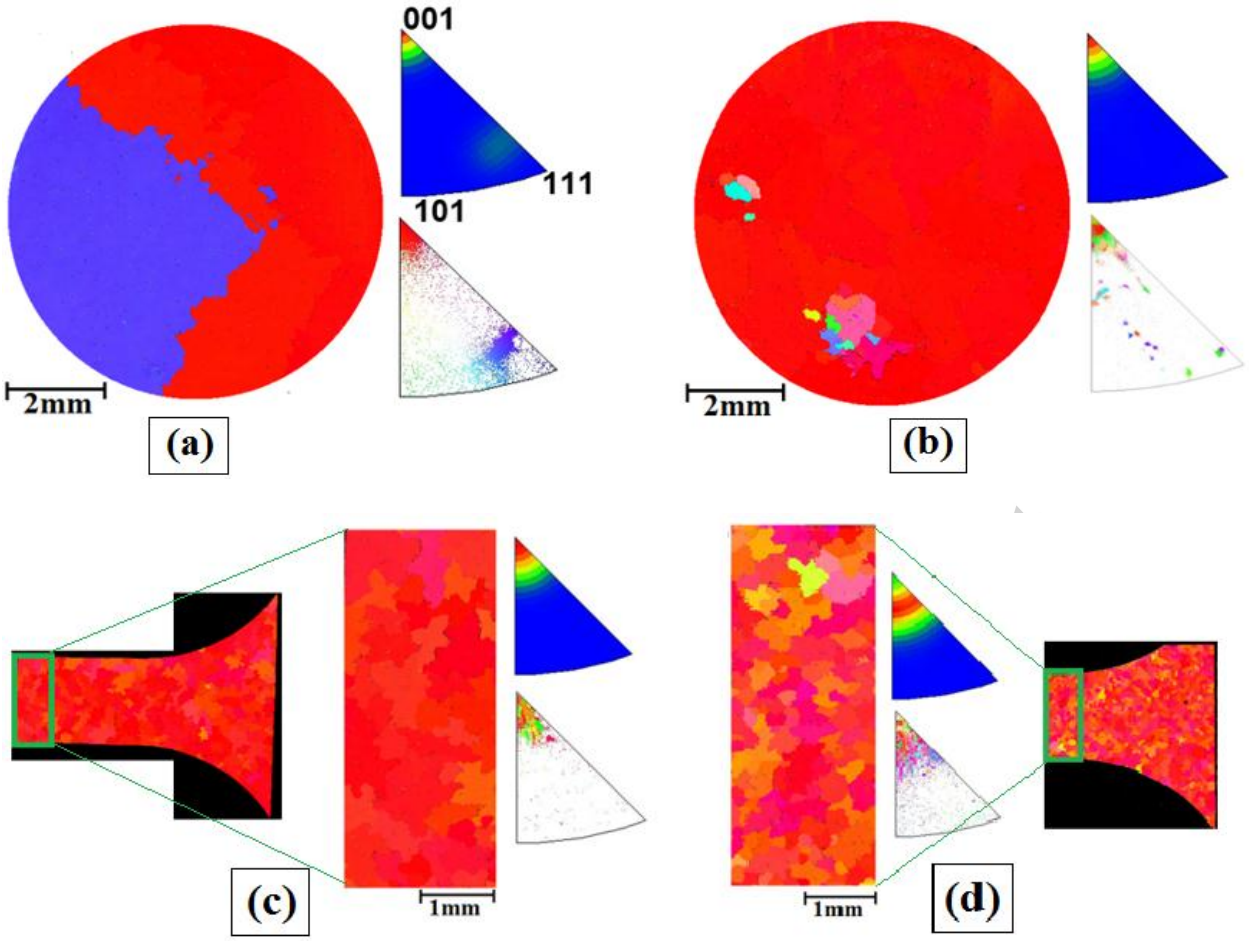

Figure 6, EBSD images, with colours showing grain orientations, for specimens subjected to 2s-2s-2s-2s (*a* and *c*) and 200s-200s-200s-200s (b and d) loading waveforms parallel (a and b) and perpendicular (c and d) to solidification direction.

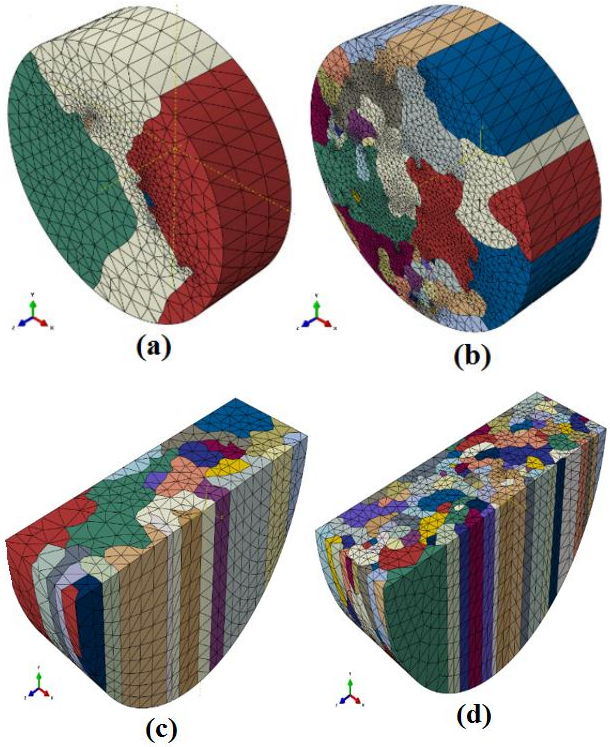

Figure 7, Developed FE models, with realistic grain structure, for specimens subjected to 2s-2s-2s-2s (a and c) and 200s-200s-200s-200s (b and d) loading waveforms parallel (a and b) and perpendicular (c and d) to solidification direction.

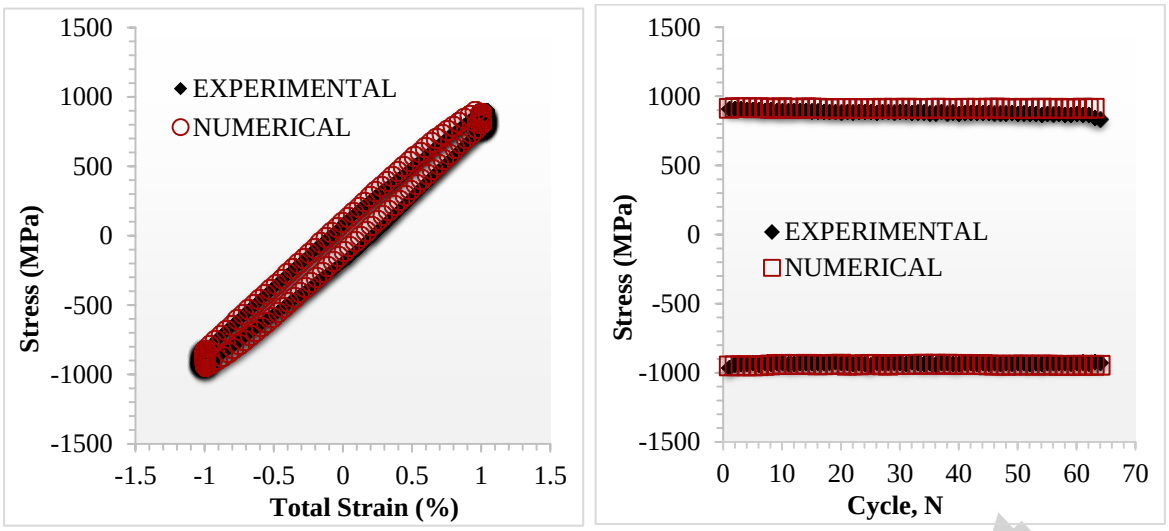

(a)

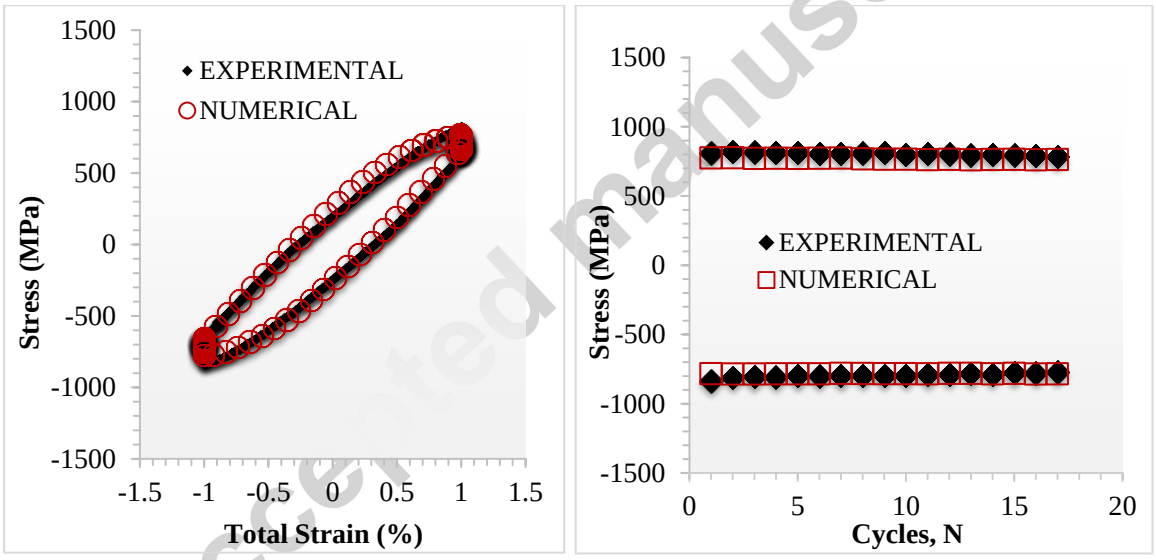

(b)

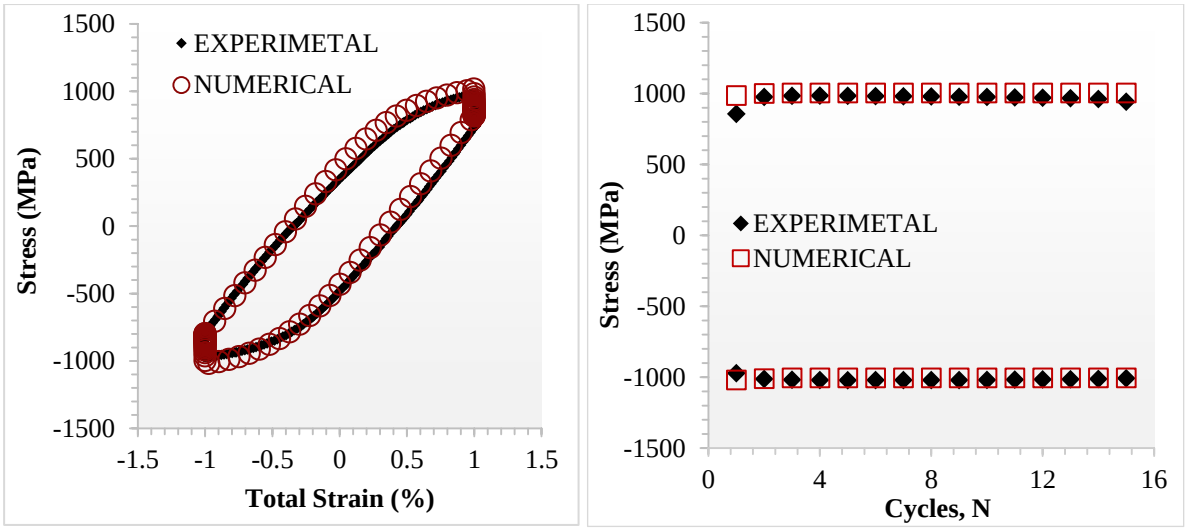

(c)

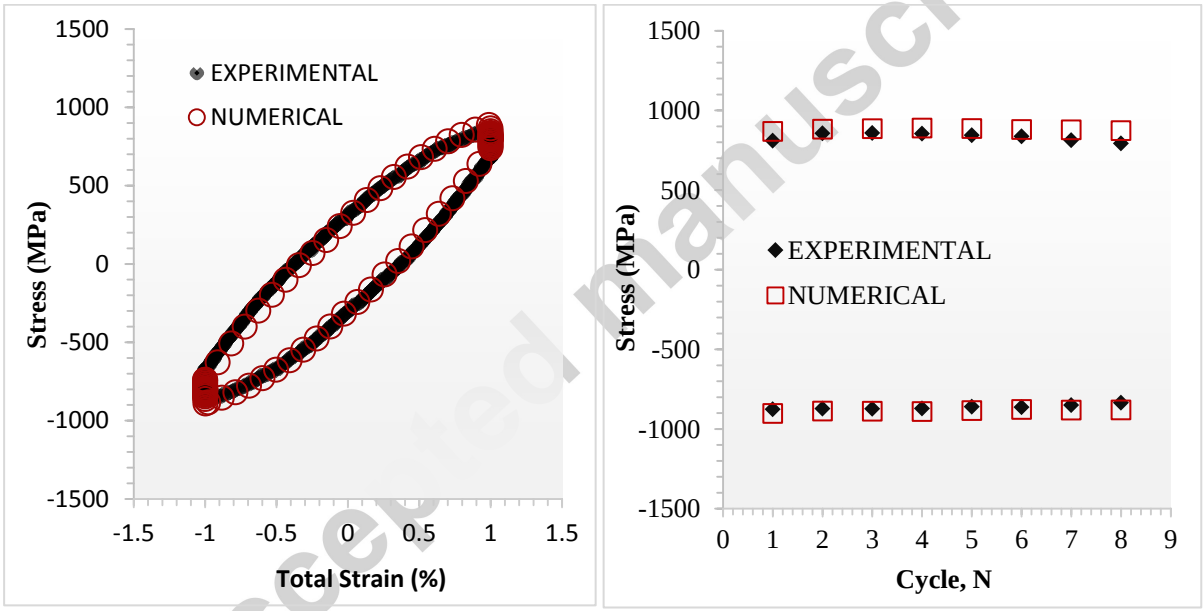

(d)

Figure 8, First stress-strain loop (left) and stress-evolution to failure (right) for 2s-2s-2s-2s (a and c) and 200s-200s-200s-200s (b and d) loading waveforms parallel (a and b) and perpendicular (c and d) to solidification direction.

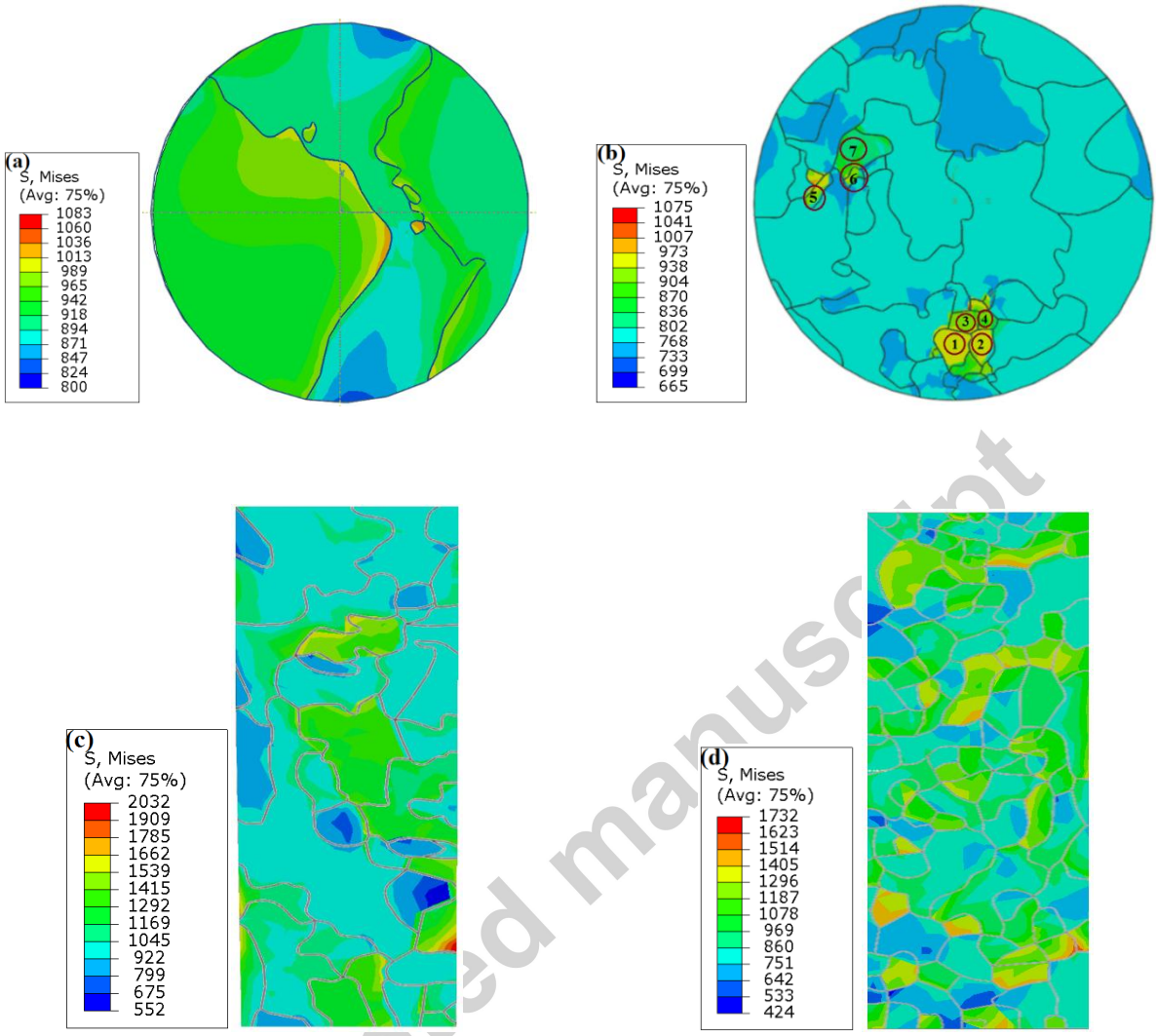

Figure 9, Contour plots of von Mises stress for specimens subjected to 2s-2s-2s-2s (a and c) and 200s-200s-200s-200s (b and d) loading waveforms parallel (a and b) and perpendicular (c and d) to solidification direction.

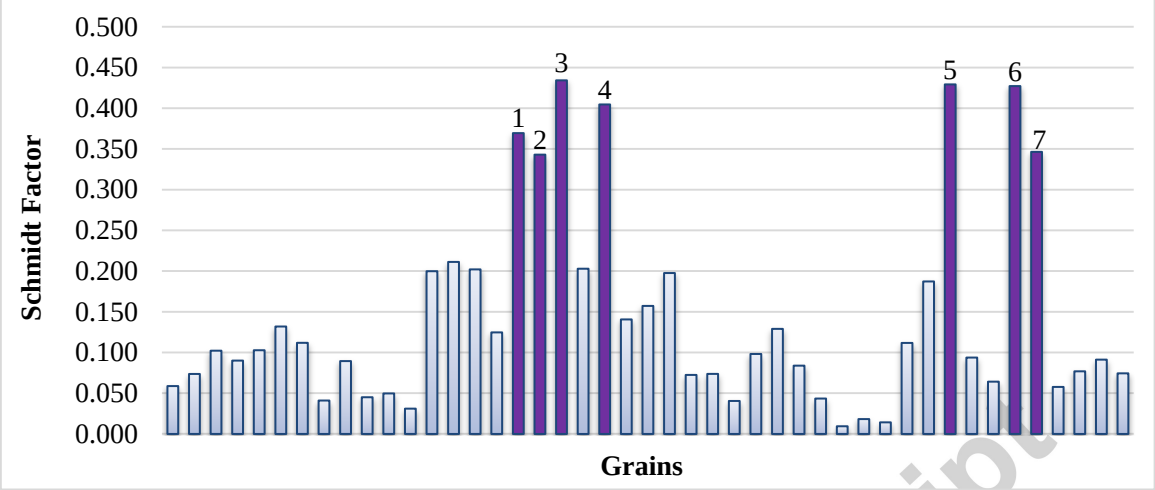

Figure 10, Schmid factors for all grains in specimen subjected to 200s-200s-200s-200s loading waveform (parallel to solidification direction).

Table 1, Nominal chemical composition by weight percentage for CM247.

Element	Al	Co	Mo	Ta	W	Cr	B	C	Zr	Nb	Ti	Fe	Cu	Hf	Ni
Weight%	5.7	9.0	0.6	3.1	9.7	8.5	0.02	0.08	0.02	0.1	0.6	0.2	0.02	1.2	Bal.

Table 2, Calibrtaed crystal plasticity model parameters.

Parameter (units)	Octahedral slip
C_{11} (GPa)	154.84
C_{12} (GPa)	87.86
C_{44} (GPa)	134.63
$\hat{\boldsymbol{\tau}}_{\mathbf{0}}$ (MPa)	1350.0
F_0 (kJ mol^{-1})	235.0
p	0.40
q	1.20
$\dot{\boldsymbol{\gamma}}_{\mathbf{0}}$ (s^{-1})	120.0
S_0 (MPa)	300.0
f_C	0.42
h_B (GPa)	195.0
h_S (GPa)	12.0
d_D	2562.37
r_D	201.63

Table 3, Euler angles for seven grains with high Schmid factors identified in specimen subjected to 200s-200s-200s-200s loading waveform (parallel to solidification direction) (see Fig. 9b)

Grain Number	ϕ_1	Φ	ϕ_2	Calculated Schmid factor
1	3.9	47.8	47.9	0.3695
2	32.6	47.7	43.5	0.3431
3	134.3	34.7	68.1	0.4343
4	135.4	29	72.7	0.4047
5	355.2	46.9	59.4	0.4294
6	64.2	31.8	72.7	0.4273
7	280.0	21.9	87.0	0.3465